coatings

IMPACT FACTOR 3.4

CITESCORE 6.1

Article

Dry Sliding Wear Behaviour of Laser Cladded AlTiSiCrCo High Entropy Alloy Coatings on Ti6Al4V: Influence of Cr/Co and Al/Ti Enrichment

Kabelo Matome Raselabe, Mamookho Elizabeth Makhatha, Nkutwane Washington Makoana and Samuel Skhosane

Special Issue
High-Entropy Alloy Films and Coatings

Edited by
Dr. Carlos G. Garay Reyes and Dr. Roberto Martínez Sánchez

MDPI

https://doi.org/10.3390/coatings16080916

coatings

MDPI

Article

Dry Sliding Wear Behaviour of Laser Cladded AlTiSiCrCo High Entropy Alloy Coatings on Ti6Al4V: Influence of Cr/Co and Al/Ti Enrichment

Kabelo Matome Raselabe [1,*], Mamookho Elizabeth Makhatha [1], Nkutwane Washington Makoana [2] and Samuel Skhosane [2]

[1] Department of Metallurgy, School of Metallurgy Mining and Chemical Engineering, University of Johannesburg, Johannesburg 2028, South Africa; emakhatha@uj.ac.za
[2] National Laser Centre, Council for Scientific and Industrial Research, Meiring Naude Road, Pretoria 0184, South Africa; nmakoana@csir.co.za (N.W.M.); sskhosane@csir.co.za (S.S.)
* Correspondence: raselabek@gmail.com

Highlights

What are the main findings?

- Laser-clad AlTiSiCrCo HEA coatings form a BCC matrix with hard intermetallic phases.
- HEA 2 (Cr/Co rich) reached 755 HV, which is 2.2 times harder than the Ti6Al4V substrate.
- All three coatings wear rate against Ti6Al4V substantially improved at 5 N and 15 N.
- HEA 2 gives the lowest wear rate, which was due to a protective Cr_2O_3 film at both 5 N and 15 N.
- Wear resistance ranking of the study is as follows: HEA 2 > HEA 3 > HEA 1 at both loads (5 N and 15 N).

What are the implications of the main findings?

- Cr/Co enrichment best describes the tribological enhancement of AlTiSiCrCo HEA system.
- Laser-cladded AlTiSiCrCo HEA coatings are a viable wear protection for Ti6Al4V substrates.
- Compositional variation of AlTiSiCrCo HEA system can shift the wear mechanism from delamination toward oxide-limited wear.
- The results give a guide in HEA coating design for sliding contact use.

Abstract

This study investigated how compositional variation within the AlTiSiCrCo high-entropy alloy (HEA) system affects the microstructure, hardness, and dry sliding wear behaviour of laser-cladded coatings on Ti6Al4V. Three coatings, namely, equiatomic (HEA 1), Cr/Co-enriched (HEA 2), and Al/Ti-enriched (HEA 3), were characterized by SEM, EDS, XRD, and Vickers microhardness and tested for dry sliding wear using a ball-on-disc tribometer at 5 N and 15 N. All coatings comprise a BCC solid solution matrix reinforced by intermetallic precipitates. HEA 2 and HEA 3 gave the highest hardness (755 HV and 754 HV, respectively) against 705 HV for HEA 1 and 345 HV for the Ti6Al4V substrate. All HEA coatings reduced wear rate relative to Ti6Al4V; HEA 2 recorded the lowest rate (4.570×10^{-5} mm^3/N.m and 2.744×10^{-4} mm^3/N.m at 5 N and 15 N, respectively), well below the substrate (2.257×10^{-4} mm^3/N.m and 0.0014 mm^3/N.m at 5 N and 15 N, respectively). Worn surface analysis showed abrasive/delamination at 5 N transitioning to more severe abrasive, adhesive, and delamination wear at 15 N. The enhanced wear resistance of

Academic Editor: Carlos G. Garay Reyes

Received: 2 July 2026
Revised: 24 July 2026
Accepted: 28 July 2026
Published: 1 August 2026

HEA 2 stems from the BCC solid solution strengthening, intermetallic reinforcement, and high chromium content, which aids in the formation of the Cr_2O_3 protective oxide film. Overall, enriching the coating with chromium and cobalt proved to be the most effective approach for improving the tribological performance of laser-cladded AlTiSiCrCo HEA coatings on Ti6Al4V.

Keywords: laser cladding; high entropy alloy; Ti6Al4V; wear rate; AlTiSiCrCo; BCC solid solution; intermetallic

1. Introduction

Industries such as aerospace, biomedical, and automotive make use of Ti6Al4V extensively due to its excellent properties such as low density, high specific strength, and corrosion resistance [1,2]. Hence, it accounts for half of all titanium alloy production globally [3]. Nevertheless, the application of Ti6Al4V under severe tribological conditions and high temperatures remains limited by its inherent poor wear resistance and low surface hardness [3,4]. Wear is a surface-initiated phenomenon; therefore, material replacement is neither economical nor the best strategy to remedy the poor tribology of Ti6Al4V. Therefore, surface engineering methods have emerged as an alternative that is cost-effective and extends the lifespan of Ti6Al4V components under demanding contact conditions [5].

Among the various surface engineering processes, which include thermal spraying, physical vapor deposition, chemical vapor deposition, and plasma nitriding [6]. Laser cladding offers a notably high-performance processing route when compared to the above-mentioned surface engineering techniques. The advantage of laser cladding is primarily attributed to the use of high energy density of the laser beam to rapidly fuse a preplaced or delivered feedstock onto a substrate, which generates a metallurgically bonded coating with minimal heat-affected zone (HAZ) and negligible substrate dilution [7,8]. The heating and cooling rates associated with laser cladding promote the formation of fine, non-equilibrium microstructures that are not attainable through conventional processing, thereby offering opportunities that can be tailored in the wear enhancement of Ti6Al4V [9,10]. Several studies have achieved wear enhancement of Ti6Al4V using laser cladding technology, Wen et al. [11] used Cr_3Cr_2-Ti6Al4V-reinforced coatings on Ti6Al4V substrate, and the coating achieved a maximum hardness of 1155.2 HV, and the wear rate was reduced by 0.74–0.86 times compared to the substrate. The wear mechanism moved from abrasive and oxidation wear due to the hard phases acting as a skeleton for oxide films. Adesina et al. [12] used Ti-Co coatings, which improved hardness and wear resistance twofold due to the formation of intermetallic phases like $CoTi_2$ and $AlTi_2$. While Zhang et al. [13] demonstrated an improved wear and hardness with elevated corrosion resistance, which was attributed to the fine-grained microstructure and hard phases formed ($CoTi_2$, $Co_{0.5}Cr_{1.5}Ti$).

High entropy alloys (HEAs) are multicomponent alloys containing five or more principal elements in equimolar or near-equimolar ratios [14]. HEA has attracted scientific interest since its inception by Cantor et al. [15]. The entropy of mixing associated with HEAs is sufficiently high to thermodynamically favour the formation of solid solution body-centered cubic (BCC) and face-centered cubic (FCC) over intermetallic compounds. In certain instances, the intermetallic compounds are formed due to the entropy and enthalpy contributions in a certain alloy system [16–18]. The formation of solid solutions and intermetallic compounds in HEAs often exhibits a combination of properties, including high hardness, thermal stability, and resistance to wear, corrosion, and oxidation [19,20], rendering HEAs as protective coating materials for tribologically demanding applications. Meng et al. [21] used TiZrNbCrCo HEA coating on Ti6Al4V via a laser cladding process.

In this study, a BCC solid solution phase with refined dendritic structures formed, and increasing the Co and Zr content raised the microhardness to 747.7 HV (2.33 times the substrate), and wear volume was reduced by 68.6%. The solid solution formation of BCC and intermetallic compounds of laser-cladded AlCoCrCuFeNi HEA on Ti6Al4V improved the wear resistance 2.62 times, and hardness increased three times that of the substrate [22]. Ren et al. [23] applied a NbMoTaWTi HEA coating using laser cladding on a titanium alloy substrate, resulting in a single BCC phase with fine dendrites that increased microhardness by 72% (600 HV) and reduced the specific wear rate by 121.9% with oxidative and adhesive wear as primary mechanisms. Despite these promising investigations on HEA coatings on Ti6Al4V via laser cladding, systematic investigations examining the influence of alloy composition variation within a single HEA (AlTiSiCrCo) family on the dry sliding wear performance of laser-clad coatings on Ti6Al4V remain limited in open literature. No study has explored how to shift elemental ratios within the AlTiSiCrCo system by enriching either the Cr/Co pair or the Al/Ti pair and how it affects the tribological behaviour on Ti6Al4V.

The present study addresses this gap by investigating the dry sliding wear behaviour of three compositions of AlTiSiCrCo-based HEA coatings, namely equiatomic $Al_{20}Ti_{20}Si_{20}Cr_{20}Co_{20}$, Cr/Co-rich $Al_{10}Ti_{10}Si_{10}Cr_{35}Co_{35}$, and Al/Ti-rich $Al_{35}Ti_{35}Si_{10}Cr_{10}Co_{10}$ onto the Ti6Al4V under normal loads of 5 N and 15 N. The aim of this study was to investigate the influence of three AlTiSiCrCo HEA compositions on microstructure, phase evolution, hardness, and dry sliding wear behaviour of laser-cladded coatings deposited on Ti6Al4V. The findings provide insight into the relationship between alloy composition and tribological performance and offer guidance for the design of HEA coatings for demanding wear-resistant engineering applications.

2. Materials and Methods

2.1. Powder Preparation and Substrate Material

The coating materials for laser cladding were prepared by mixing elemental powders of Al, Ti, Si, Cr, and Co with ≥99.9% purity and particle size ranging from 45 to 100 µm. The elemental powders were procured from Weartech Pty Ltd. (Wadeville, South Africa). (Al, Ti) and LGC Industrial Analytical Pty Ltd. (Johannesburg, South Africa). (Si, Cr, and Co). The three coatings investigated in this study were an equiatomic AlTiSiCrCo (HEA 1), a Cr/Co-enriched composition $Al_{10}Ti_{10}Si_{10}Cr_{35}Co_{35}$ (HEA 2), and an Al/Ti-enriched composition $Al_{35}Ti_{35}Si_{10}Cr_{10}Co_{10}$ (HEA 3).

The nominal composition of each powder mixture, expressed in atomic percentage (at%) and the corresponding weight percent (wt%), is given in Table 1. The elemental powders for each coating were weighed to these ratios prior to mixing. The powders were mechanically blended using a tubular mixer inside a stainless steel at 300 rpm for 8 h to ensure compositional homogeneity before laser cladding.

Table 1. Nominal composition of the elemental powder mixtures used for laser cladding.

Coatings	Al	Ti	Si	Cr	Co
HEA 1 (at%/wt%)	20/12.6	20/22.4	20/13.1	20/24.3	20/27.6
HEA 2 (at%/wt%)	10/5.5	10/9.7	10/5.7	35/37.1	35/42.0
HEA 3 (at%/wt%)	35/23.6	35/41.8	10/7.0	10/13.0	10/14.7

The substrate plate of Ti6Al4V has dimensions of 150 mm × 50 mm × 6 mm. The nominal composition of the Ti6Al4V substrate is Ti (balance), Al 6.01 wt%, V 3.84 wt%, Fe 0.30 wt%, Si 0.15 wt%, O 0.15 wt%, C 0.10 wt%, and N 0.15 wt%. The Ti6Al4V was supplied by Zhejian Shenji Titanium Industry Co., Ltd. (Huzhou City, China). in an annealed

condition. Prior to laser cladding, the Ti6Al4V substrate surface was sandblasted to reduce laser radiation and subsequently cleaned with ethanol to remove surface contaminants and ensure good metallurgical bonding between the coating and the Ti6Al4V substrate. A schematic overview of the overall experimental flow and laser-cladded HEA coatings is shown in Figure 1.

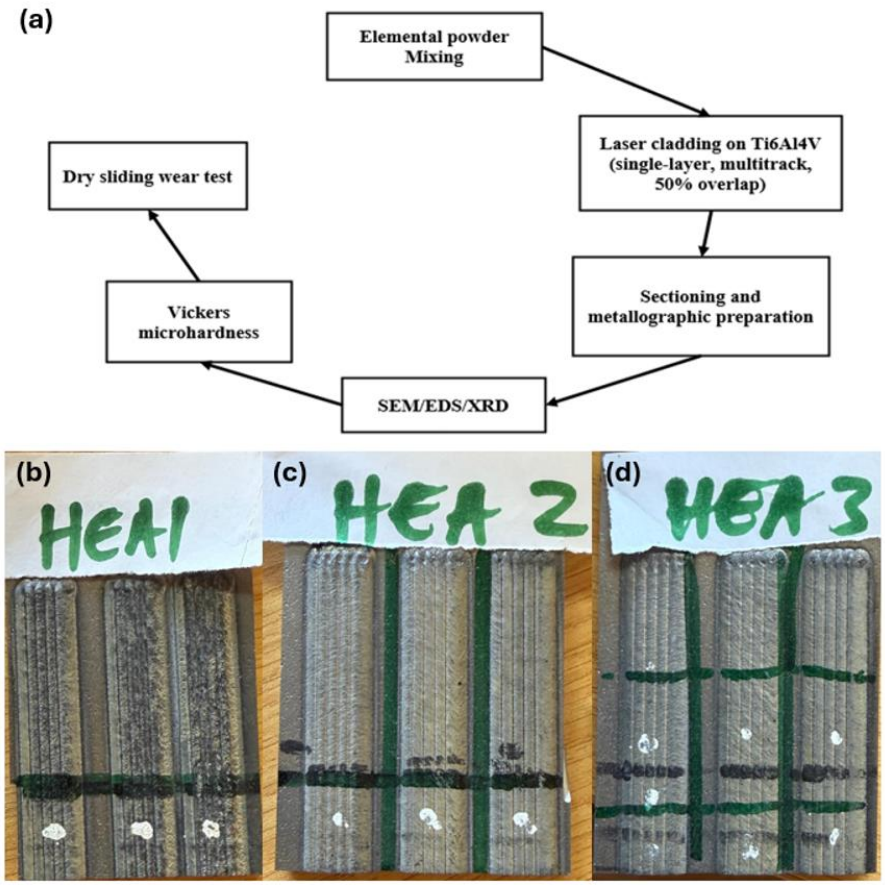

Figure 1. Showing (**a**) Schematic overview experimental flow and (**b**) HEA 1, (**c**) HEA 2 and (**d**) HEA 3 coatings.

2.2. Laser Cladding Process

The 3 kW IPG fibre laser cladding system equipped with a coaxial powder feeding nozzle was used to coat the Ti6Al4V substrate. Optimization of the process parameters was carried out to produce a defect-free coating from our previous study [24], using the response methodology (RSM) optimization tool to produce a defect-free coating. Therefore, the optimized laser cladding parameters were 0.8 kW laser power, 0.75 m/min scanning speed, 3 g/min powder feed rate, spot diameter of 2 mm, shielding gas rate of 15 L/min, and 50% overlap with a stand-off distance the laser beam set at 12 mm between substrate and nozzle. The coatings were deposited in a single layer using a multi-track scanning strategy with parallel tracks. Three coated specimens were produced for each alloy composition using identical laser processing parameters, and all specimens were ground and polished following laser cladding prior to microstructural, hardness, and wear characterization.

2.3. Microstructural Characterization

Post laser cladding, the coated samples were sectioned using a precision cutter and prepared following standard metallographic sample preparation, with Kroll's reagents (6 mL HNO_3 + 2 mL HF + 92 mL H_2O) used as etchant. The microstructural and compositional analysis was performed using a JEOL JSM-7900F scanning electron microscope (SEM,

Tokyo, Japan) equipped with an energy-dispersive spectrometer (EDS, Oxford Instruments, Abingdon, UK). Phase identification was carried out by X-ray diffraction (XRD) analysis using PANalytical X'Pert Pro (Almelo, The Netherlands) operated at 40 KV, and 20 mA, with diffraction patterns recorded over the 2θ range of 10–80° with a step size of 0.02° using Cu-Kα radiation (λ = 1.5406 Å). All coatings measured 810–960 μm thick (Section 3.1), and XRD was performed on the as-polished top surface of the coating rather than after coating removal. Therefore, the peaks detected in XRD data are 100% coatings and not Ti6Al4V substrate. Coating thickness was measured from the cross-sectional samples using an Olympus BX41M-Led optical microscope (Tokyo, Japan), with a minimum of five measurements taken at different locations along each coating to represent an average value. Optical microscopy provides sub-micrometer resolution, which is more than adequate for coatings of this thickness (800–960 μm), and allowed rapid averaging of five measurements per coating across the full cross-section width. SEM was reserved for the higher resolution microstructural and EDS phase analysis where its greater resolution is necessary.

2.4. Microhardness Measurements

The Vickers microhardness measurements were performed using a load of 500 g ($HV_{0.5}$) and a dwell time of 15 s. Ten indentations were made across the cross section of each specimen, beginning within the coating region and progressing towards the substrate at 0.5 mm spacing, large enough to prevent interaction between adjacent plastic deformation zones. The average coating hardness and standard deviation were calculated from the indentations located entirely within the coating.

2.5. Dry Sliding Wear Testing

The dry sliding wear test was performed on the three coatings and Ti6Al4V substrate using a ball-on-disk Anton Paar tribometer (Graz, Austria). The counter body was an Al_2O_3 ball with a diameter of 6 mm. The wear test was performed under normal loads of 5 and 15 N, at a sliding speed of 7.50 cm/s and a total distance of 250 m at room temperature. The two loads were selected to evaluate the tribological behaviour of the coatings under representative mild and severe sliding conditions and investigate the influence of increasing load on wear performance and wear mechanisms. The friction coefficient was recorded for each test, and the average was recorded. Following the wear test, the wear volume (V) loss was determined from mass loss Δm (measured with an analytical balance, sensitivity 1×10^{-5} g) using.

$$V = \frac{\Delta m}{\rho} \quad (1)$$

where ρ is the coating density. The densities used were HEA 1 = 5.11 g/cm^3, HEA 2 = 6.56 g/cm^3, and HEA 3 = 4.36 g/cm^3. The theoretical rule of mixture from the nominal composition was used to determine the coating densities used in Equation (1). The specific wear rate was subsequently calculated according to the following expression in Equation (2):

$$W = \frac{V}{F \times L} \quad (2)$$

where W is the specific wear rate (mm^3/N.m), V is the wear volume loss (mm^3), F is the applied normal load (N), and L is the total sliding distance (m). The worn surface morphologies of the laser-clad HEA coatings and the Ti6Al4V substrate were examined by SEM analysis to identify the wear mechanism and characterize oxide layer development and material transfer at both loads.

3. Results and Discussions

3.1. Coating Thickness Analysis

The average coating thickness measured by optical microscopy for HEA coatings are 960.67 µm (HEA 1), 897.17 µm (HEA 2), and 810.14 µm (HEA 3) in Figure 2. HEA 1 produced the thickest coating, HEA 2 an intermediate value, and HEA 3 the thinnest coating amongst all the coatings. This difference is attributed to the compositional dependence of melt-pool dynamics during laser cladding; the changes in elemental ratios of Al, Ti, Si, Cr, and Co affect the liquidus temperature and viscosity of the melt pool, which in turn govern clad height and dilution depth. HEA 3 coatings with high Al and Ti content exhibit increased melt pool fluidity owing to lower melting points of these elements, resulting in greater spreading and reduced clad height. Conversely, the elevated Cr and Co of HEA 2 have higher melting points and are known to increase melt pool viscosity by promoting thicker deposits under equivalent processing conditions [22]. HEA 1 with the highest coating thickness reflects the equiatomic balance between these opposing tendencies. Although minor variations in coating thickness were observed among the three HEA compositions, all coatings exceed 800 µm and therefore provided complete substrate coverage during wear tests. The differences in thickness are attributed to compositional effects on melt pool viscosity, wetting behaviour, and solidification characteristics rather than differences in laser processing parameters, which were kept constant throughout the study. The differences in tribological performance are primarily attributed to the effects of alloy composition and microstructure rather than thickness.

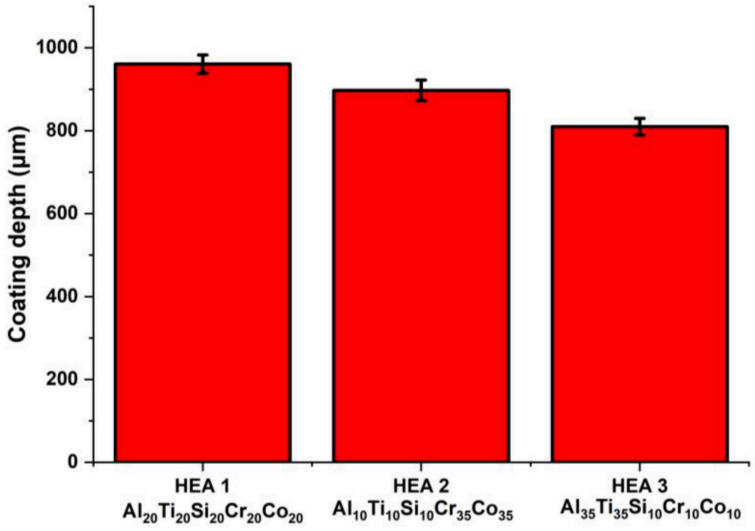

Figure 2. Average coating thickness of the HEA coatings.

3.2. Phase and Microstructural Analysis

The XRD patterns of the three laser cladded coatings are presented in Figure 3, with the identified reflections indexed in Table 2. All coatings contain a BCC solid solution together with multiple intermetallic compounds. In HEA 1, the equiatomic composition, the XRD peaks revealed the presence of an intermetallic $Al_{13}Co_4$ at $2\theta = 25.05°$, overlapping intermetallics of $Cr_2Ti/AlSi_3Ti_2$ at $2\theta = 36°$ and BCC reflections at $2\theta = 40°$, 42.2° and 43.5°. The formation of the $Al_{13}Co_4$ intermetallic in an equiatomic alloy is thermodynamically driven by the strongly negative ($\Delta Hmix = -19$ kJ/mol), which is sufficient to overcome the configurational entropy stabilisation. This is analogous to the behaviour of $(Ti, V)_5Si_3$ reported by Huang et al. [25] in TiVCrAlSi coatings, where the enthalpy of silicide formation is shown to offset the entropy term in the Gibbs free energy balance. The co-presence of $AlSi_3Ti_2$ and Cr_2Ti at 36° reflection further demonstrates that Si in the equiatomic

composition has sufficient activity to form silicide phases. The BCC phases are attributed to Ti-Cr-Al solid solutions, which are formed by BCC-stabilising elements (Al, Cr, and Ti) consistent with the phase constitution reported for HEA coatings by Prabu et al. [22].

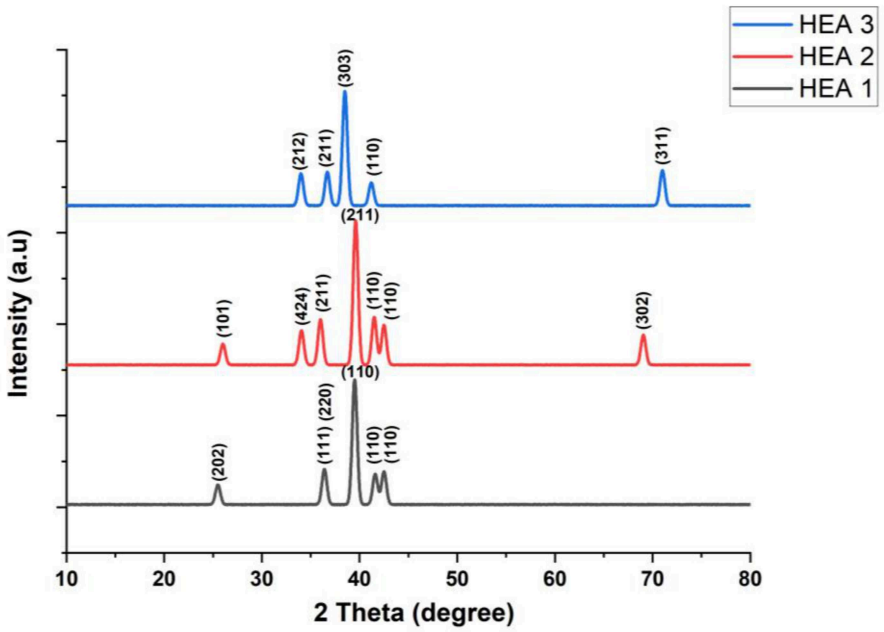

Figure 3. Showing XRD patterns of the laser-cladded HEA coatings on Ti6Al4V.

HEA 2 presented XRD dominant BCC reflections at 2θ = 36°, 39.5°, 42.3°, and 43.5° alongside $AlTi_3$ (2θ = 26.01°, 69.05°) and $AlCr_2$ (2θ = 34.05°). The enrichment of Cr and Co at the expense of Al, Ti, and Si suppresses the intermetallic-forming tendency observed in HEA 1, leading to a mostly BCC microstructure. The formation of $AlTi_3$ indicates partial segregation of Al and Ti during solidification, which is consistent with relatively lower Al content in HEA 2 limiting solid solution of Al within the BCC lattice. The presence of $AlCr_2$ reflects the high chemical affinity between Al and Cr (strongly negative $\Delta Hmix = -10$ kJ/mol). The dominant BCC constitution of HEA 2 is expected to contribute positively to hardness and wear resistance, as the BCC phase offers fewer slip systems than FCC, thereby resisting plastic deformation under tribological conditions [26].

HEA 3 presented an XRD pattern showing BCC reflections at 2θ = 35.8° and 42.3°, an $AlCr_2$ peak at 34.5°, $Al_{13}Co_4$ at 37.5° and $AlTi_3$ at 70.2°. The emergence of $AlCr_2$, $Al_{13}Co_4$ and $AlTi_3$ together with the absence of any silicide reflections indicates that the elevated Al and Ti contents direct intermetallic formation towards Al-Cr, Al-Co, and Al-Ti compounds rather than Si-bearing phases. The reduced Si content (10 at%) relative to HEA 1 (20 at%) appears insufficient to sustain silicide precipitation at rapid cooling rates associated with laser cladding. Overall, the XRD confirms that none of the HEA coatings is a single solid solution, and all exhibit BCC with secondary intermetallic phases. This is consistent with the widely reported finding that thermodynamic interactions between configurational entropy and mixing enthalpy govern whether simple solid solutions or intermetallic compounds form in HEA systems [27,28]. Certain reflections assigned to higher-order BCC indices (211) occur at lower 2θ than corresponding (110) reflections, which is not expected for a single BCC phase. This most likely indicates that each coating contains more than one BCC solid solution phase of slightly differing lattice parameters, a consequence of compositional micro-segregation during rapid solidification. Each peak was matched independently to its ICDD reference pattern rather than assigned within a single lattice framework. Confirming this would require full crystallographic refinement (Rietveld analysis), a wider 2θ scan, and EBSD/TEM phase mapping, which were beyond the scope

of the present characterization and are recommended as follow-up work. Phases supported by only one or two reflections (Table 2) should accordingly be regarded as tentative.

Table 2. XRD peak indexing of the identified phases in the three laser cladded HEA coatings.

HEA Coating	2θ (°)	Phase	hkl	ICDD Card No
HEA 1 [29]	25.05	$Al_{13}Co_4$	202	000500786
	36	$AlSi_3Ti_2/Cr_2Ti$	111/220	000561144/010717626
	40	BCC	110	030659021
	42.2	BCC	110	010717488
	43.5	BCC	110	030656108
HEA 2	26.01	$AlTi_3$	101	000520859
	34.05	$AlCr_2$	424	010734629
	36	BCC	211	010717488
	39.5	BCC	211	010702876
	42.3	BCC	110	010717488
	43.5	BCC	110	030656108
	69.05	$AlTi_3$	302	010744579
HEA 3	34.5	$AlCr_2$	424	010734629
	35.8	BCC	211	010702876
	37.5	$Al_{13}Co_4$	303	000500786
	42.3	BCC	110	010717488
	70.2	$AlTi_3$	311	000520859

Figure 4 is a representation of SEM micrographs of the three coatings. In all compositions, the microstructure consists of a matrix phase with secondary precipitates or interdendritic constituents, reflecting the rapid solidification associated with laser cladding. The coatings appear metallurgically bonded with the Ti6Al4V substrate, with no gross porosity or delamination visible at the interface. The EDS elemental analysis results summarized in Table 3 provide compositional detail of the identified regions in each coating. In HEA region 1, region A and region B reflect minor elemental partitioning between phases. The relatively even distribution of all five principal elements in both regions confirms near-equiatomic characteristics, with the small differences in Si and Ti content between regions A and B consistent with preferential partitioning of Ti and Cr into the BCC matrix. In HEA 2, the higher Ti in region D relative to C suggests that the Ti intermetallic $AlTi_3$ is concentrated in the interdendritic regions. In HEA 3, regions E and F both show high Al and Ti content with low Cr and Co contents, which is consistent with the Al/Ti-enriched nominal composition. The near uniform distribution between E and F implies a more homogeneous microstructure in HEA 3. The low content of V in all coatings originates from partial dilution of the Ti6Al4V substrate.

The coating-substrate transition zone was examined using the EDS line scans in Figure 5. All three coatings show a continuous compositional gradient, a progressive increase in Ti and V, and a corresponding decrease in Al, Cr, Co, and Si over the last 3–4 μm of the scan rather than an abrupt compositional boundary, consistent with the gradual hardness transition noted in Figure 6a. This indicates the transition zone in all three coatings is described as a dilution zone produced by melting and diffusion of the Ti6Al4V substrate into the melt pool rather than a distinct interfacial phase. Site-specific

phase identification within this zone by EBSD or TEM was not performed in the present study and is recommended for future work on this coating system.

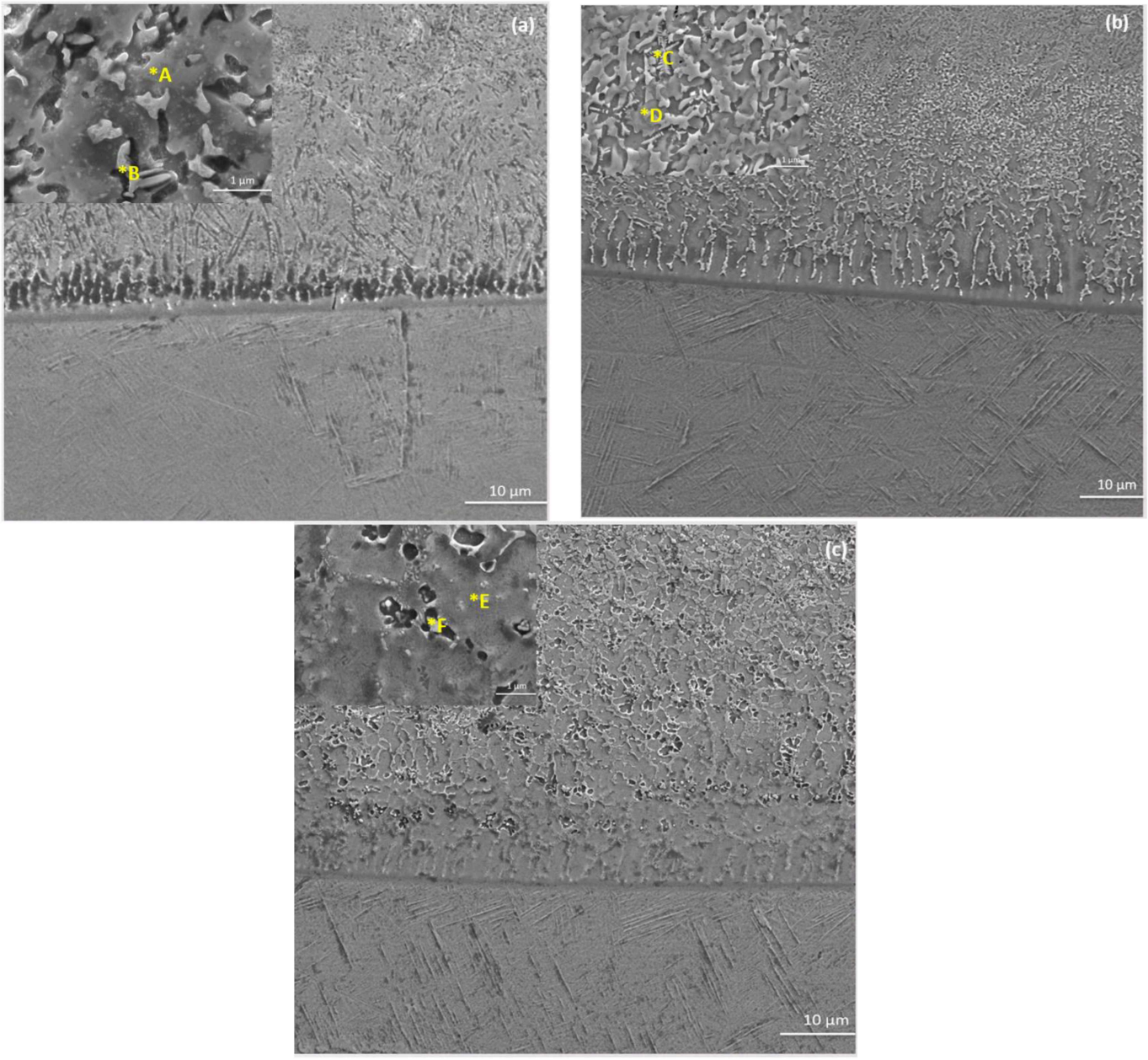

Figure 4. SEM images of (**a**) HEA 1 Reprinted from Reference [29], (**b**) HEA 2, and (**c**) HEA 3 coatings with EDS spot analysis for HEA 1 (*A, *B), HEA 2 (*C, *D) and HEA 3 (*E, *F).

Table 3. EDS compositional analysis of microstructural regions in the three HEA coatings (wt% and at%).

Alloy	Region	Al	Ti	Si	Cr	Co	V	Unit
HEA 1	A	20.1	24.1	17.5	18.4	19.0	0.9	wt%
		22.4	18.9	18.8	10.7	9.7	0.5	at%
	B	17.2	30.1	12.1	22.9	17.7	0	wt%
		19.0	18.9	13.9	13.3	9.0	0	at%

Table 3. *Cont.*

Alloy	Region	Al	Ti	Si	Cr	Co	V	Unit
HEA 2	C	10.2	12.6	8.5	34.5	33.8	0.4	wt%
		11.8	7.9	9.4	20.0	17.3	0.2	at%
	D	7.3	18.4	7.6	32.5	34.2	0.5	wt%
		8.5	11.6	8.5	19.0	17.5	0.3	at%
HEA 3	E	37.7	43.9	3.8	7.1	7.2	0.3	wt%
		42.0	27.6	4.1	4.1	3.7	0.2	at%
	F	35.5	43.5	4.2	7.2	8.8	0.8	wt%
		39.7	27.4	4.5	4.2	4.5	0.5	at%

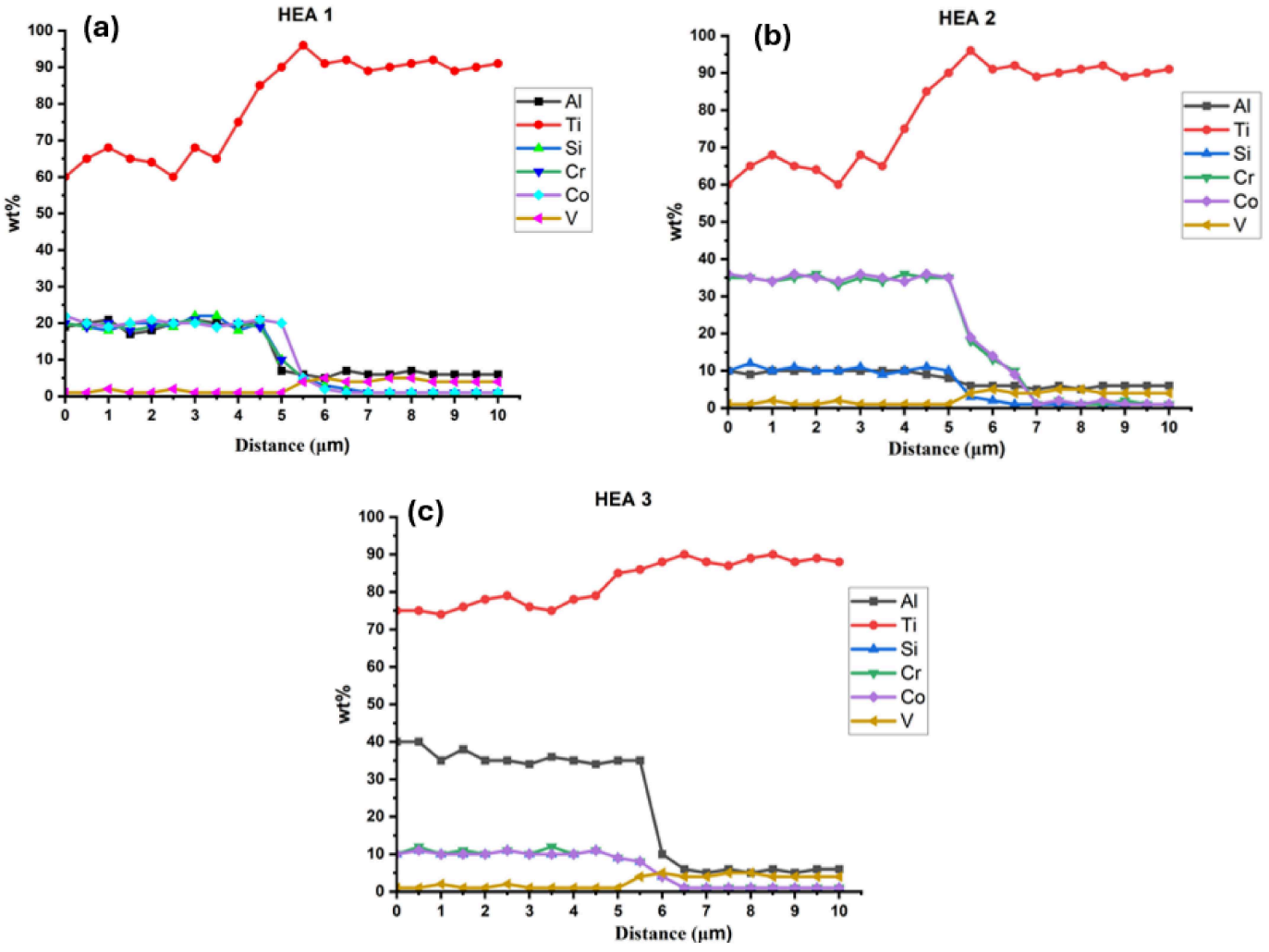

Figure 5. EDS line scanning results along the cross-sectional path of (**a**) HEA 1, (**b**) HEA 2 and (**c**) HEA 3 coating.

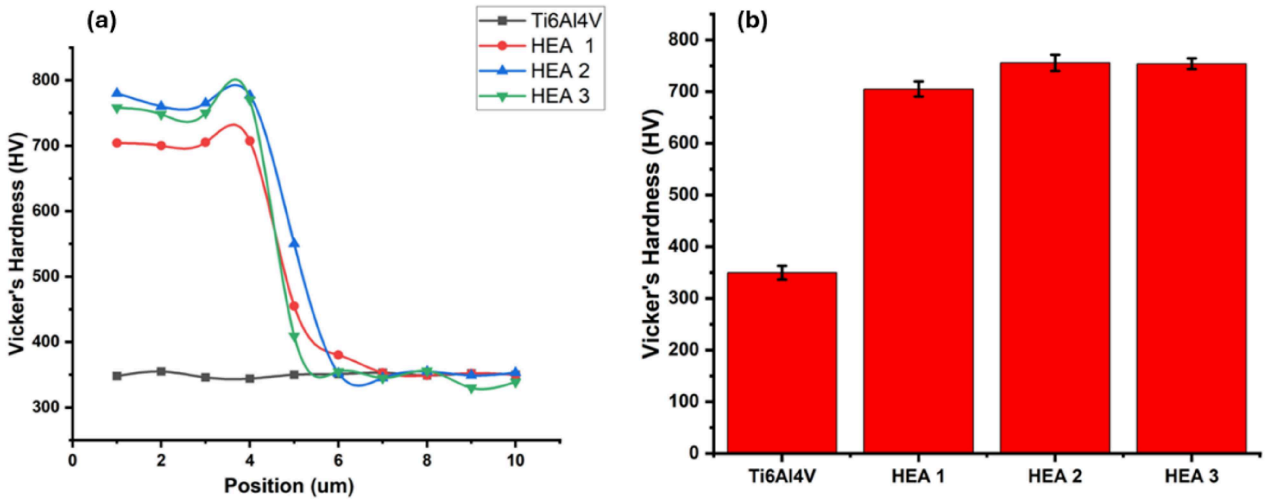

Figure 6. Showing (**a**) hardness profile across the Ti6Al4V substrate and (**b**) average hardness of Ti6Al4V vs. HEA coatings.

3.3. Hardness Evaluation

The Vickers hardness microhardness profiles and average coating hardness values are presented in Figures 6a and 6b, respectively. All the HEA coatings in this study exhibit substantially higher hardness than the Ti6Al4V substrate (345 ± 12 HV). The average hardness value of the HEA coatings is 705.1 ± 13.09 HV (HEA 1), 755.1 ± 15.8 HV (HEA 2), and 754.2 ± 10.39 HV (HEA 3). This enhancement of hardness demonstrates the effectiveness of laser cladding with complex multi-principal element compositions as a surface hardening strategy for Titanium alloys. The hardness profile in Figure 6a shows a gradual transition from the coating to the substrate, with a heat-affected zone of reduced hardness relative to the bulk coating observed near the interface. This gradient is a well-known characteristic of laser cladded coatings on Ti6Al4V and is due to partial dissolution and diffusion of substrate elements into the lower regions of the melt pool [30].

The enhanced hardness of the coatings relative to the Ti6Al4V substrate is due to two principal mechanisms. First, the solid solution formation arises from the severe lattice distortion generated by the simultaneous incorporation of elements with markedly different atomic radii (Al:143 pm, Ti: 147 pm, Si: 111 pm, Cr:128 pm, Co 125 pm) within the BCC lattice. This distortion impedes dislocation motion and increases resistance to plastic deformation [5,31]. The second mechanism is the dispersion hardening by the hard intermetallic precipitates identified in the XRD analysis ($Al_{13}Co_4$, $AlTi_3$, $AlCr_2$, $AlSi_3Ti_2$, and Cr_2Ti), which further contributes to the high hardness values. Among the three coatings, HEA 2 shows the highest average hardness given by its dominant BCC constitution and the presence of hard $AlCr_2$ and $AlTi_3$ intermetallics. HEA 3 exhibits an intermediate hardness amongst the three coatings, benefiting from the intermetallic of $Al_{13}Co_4$ and $AlTi_3$ with a BCC solid solution. HEA 1 benefits from silicide formation, but the equiatomic balance distributes elements across more phases, reducing the fraction of any single hard phase.

3.4. Wear Analysis

The tribological performance of the HEA coatings relative to the uncoated Ti6Al4V substrate was evaluated using a ball-on-disk sliding wear test at two normal loads of 5 N and 15 N. The coefficients of friction (CoF) and wear rate results are presented in Figures 7 and 8, respectively.

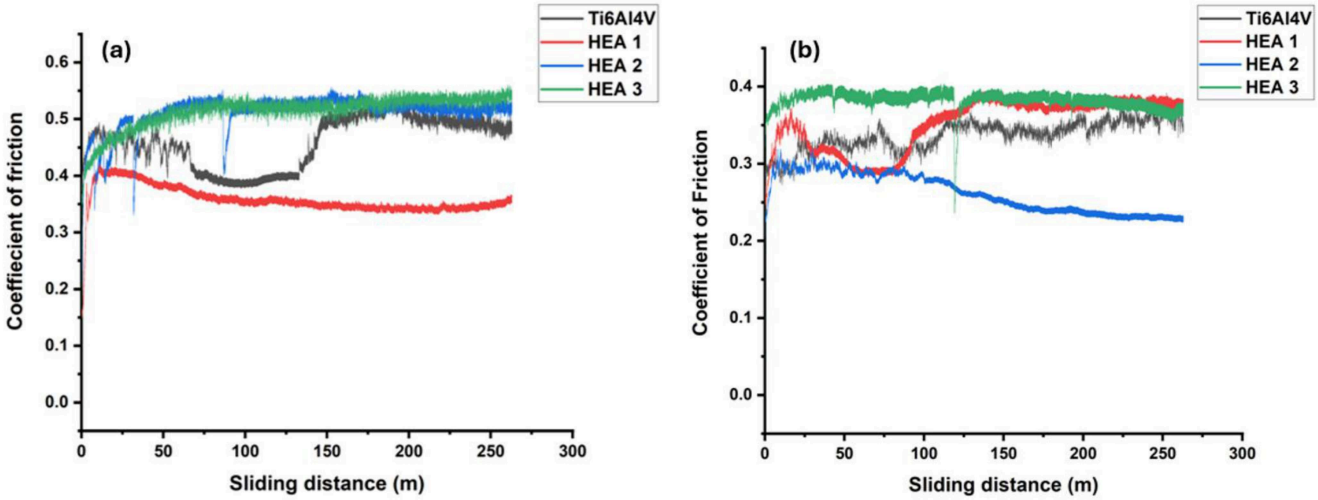

Figure 7. Coefficient of friction of Ti6Al4V vs. HEA coatings at (**a**) 5 N and (**b**) 15 N.

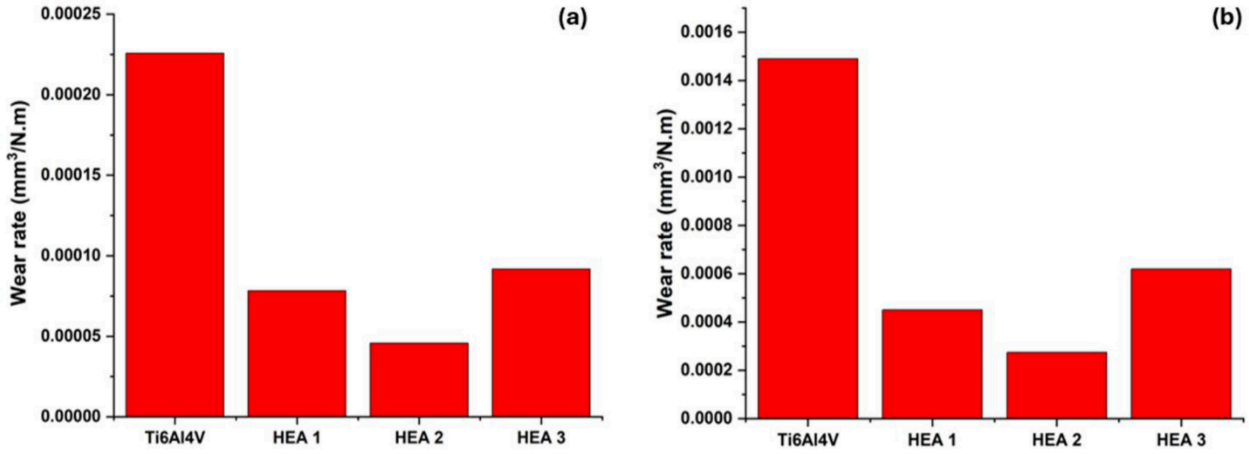

Figure 8. Wear rate of Ti6Al4V vs. HEA coatings at (**a**) 5 N and (**b**) 15 N.

The average CoF values at 5 N are 0.46 ± 0.04 for Ti6Al4V, 0.36 ± 0.03 for HEA 1, 0.51 ± 0.02 for HEA 2, and 0.52 ± 0.03 for HEA 3. At 15 N the values increased to 0.34 ± 0.05 for the Ti6Al4V substrate, 0.35 ± 0.04 for HEA 1, 0.26 ± 0.03 for HEA 2, and 0.38 ± 0.04 for HEA 3. Unlike the hardness and wear rate trends, the CoF results do not show a uniform reduction for all the HEA coatings composition relative to the substrate. At 5 N, only HEA 1 recorded a lower CoF than the substrate, HEA 2 and HEA 3 both exceeded the substrate value, indicating frictional behaviour at this load is not governed solely by hardness. Similar behaviour is seen in the work by Ren et al. [23] and Meng et al. [21], where the HEA coatings had higher CoF averages than that of the substrate. At 15 N, the reduction in CoF in HEA 2 relative to the substrate is consistent with reports of Cr-rich oxide film formation in HEA coatings under high contact stress [32,33], in which Cr_2O_3-rich layer develops at the sliding interface during frictional heating. This mechanism best defines the HEA 2 coating, given its high Cr content, which promotes Cr_2O_3 oxide film formation. This is directly supported by the EDS point analysis of the worn surface at 15 N, which shows HEA 2 retaining a Cr content of 29–34 at%, close to its nominal coating composition of 35 at%, with 9–18 at% of O at the track, consistent with a retained, oxidized Cr-rich layer rather than Cr being preferentially removed during sliding. However, this phenomenon does not translate to HEA 1 or HEA 3, whose CoF values at 15 N are comparable to or higher than the substrate's, suggesting that Cr content alone does not predict the frictional response across all the compositions.

At lower load 5 N (Figure 8), the wear rates of all three coatings are significantly below that of Ti6Al4V confirming the tribological benefit of the HEA surface treatment. Ti6Al4V resulted in a wear rate of 2.257×10^{-4} $mm^3/N.m$ as compared to HEA 1 with 7.827×10^{-5} $mm^3/N.m$, HEA 2 with 4.57×10^{-5} $mm^3/N.m$ and HEA 3 with 9.174×10^{-5} $mm^3/N.m$. The wear rate hierarchy at 5 N is expected to reflect the hardness ranking of coatings, with Cr/Co enriched HEA 2 exhibiting the lowest wear rate and HEA 3 exhibiting a slightly higher wear rate owing to its comparatively lower intermetallic hardness contribution. At the higher load of 15 N (Figure 8b), the wear rate increases across all specimens, as expected from Archard's wear law (Q = kWL/H), where the wear volume Q increases proportionally with normal load W. The dimensionless wear coefficient K, calculated from specific wear rate and hardness data (Table 4), stays within the 10^{-4}–10^{-3} range, characteristic of mild to moderate, oxidation-dominated wear at both loads, confirming that none of the coatings shift into a severe adhesive wear mechanism even at 15 N. However, the coatings continue to outperform the Ti6Al4V (0.00149 $mm^3/N.m$) substrate at 15 N, 4.500×10^{-4} $mm^3/N.m$ for HEA 1, 2.744×10^{-4} $mm^3/N.m$ HEA 2, and 6.192×10^{-4} $mm^3/N.m$ HEA 3. This load-dependant improvement in wear resistance is consistent with the work done by Zhang et al. [34]. The difference in wear rate and CoF between the two load conditions also reflects a transition in the wear mechanism. The 5 N load provided oxidative wear, which is characterised by the formation of compacted oxide layers that act as lubricants and limit direct abrasiveness. At 15 N the increased contact partially disrupts the protective oxide layer by increasing the contribution of abrasive and adhesive wear mechanisms and elevating both CoF and wear rate. This transition mechanism is consistent across various HEA coatings under high load conditions [34,35].

Table 4. Dimensionless Archard wear coefficient K, calculated from the specific wear and hardness reported in Sections 3.3 and 3.4 (K = specific wear rate × H).

Material	Hardness H (GPa)	K at 5 N	K at 15 N
Ti6Al4V	3.38	0.00076	0.0050
HEA 1	6.92	0.00054	0.0031
HEA 2	7.41	0.00034	0.0020
HEA 3	7.40	0.00068	0.0046

3.5. Worn Surface Analysis

The SEM micrographs of the worn surface at 5 N and 15 N are presented in Figures 9 and 10, respectively, and confirm the wear mechanism interpretations drawn from the friction and wear rate. At 5 N, the Ti6Al4V substrate (Figure 9a) shows a worn track characterised by a well-defined wear groove parallel to the sliding direction, abrasive track, and localised spalling. The grooves are consistent with microcutting and ploughing by the Al_2O_3 ball. This in turn confirms the abrasive wear dominance mechanism in the substrate under a 5 N load. The spalling observed at the track edges indicates fatigue damage caused by detachment of material and contact stress cycling [18].

HEA 1 coating (Figure 9b) exhibits a different worn surface, which is dominated by wear debris within the wear track, delamination, and spallation. The absence of deep directional grooves suggests that the intermetallic of HEA 1 resisted micro-cutting. The resulting delamination produces large, irregularly shaped fragments that are distributed as fine wear debris within the wear track. This delamination mechanism is further a characteristic of hard coatings in which the fracture toughness is insufficient to limit lateral crack growth despite the high hardness (705 HV) limiting penetration by the Al_2O_3. The spalling at the boundary of the track further confirms this interpretation by indicating damage extends beyond the central contact zone. HEA 2 presented a mixed wear mechanism at 5 N by

combining shallow wear grooves, delamination patches, and compacted debris layers. The co-existence of abrasive grooving and delamination features indicates a transition between the abrasive behaviour of the substrate and the delaminated behaviour of HEA 1. Further suggesting intermediate mechanical response of Cr/Co-enriched composition. The wear debris in the HEA 2 track appears finer and more uniformly distributed than in HEA 1, suggesting that debris generated during sliding is partially retained in the mechanically mixed layer (Cr_2O_3 oxide film) that reduces direct Al_2O_3 and coating surface. This is corroborated by the EDS point analysis of the worn surface at 5 N (Table 5), which shows the HEA 2 debris/track points retaining 29–35 at% Cr, essentially matching the bulk coating composition, alongside 5–19 at% O, consistent with a partially oxidized, Cr-rich debris layer rather than bare metallic debris.

HEA 3 at 5 N shows less worn track with shallow wear grooves, discrete delamination patches, and moderate debris accumulation. The track width and depth are visually smaller than those of HEA 1 and HEA 2 but show a higher wear rate amongst the HEA coatings. This discrepancy is attributed to the nature of the damage; the delamination in HEA 3 removes material in the depth direction through crack propagation parallel to the coating surface and generates mass loss without widening the visible track. The absence of a stable oxide film can be attributed to the low content of Cr to sustain Cr_2O_3 formation and the brittle nature of Al/Ti-enriched intermetallic phases. This entails that the debris is expelled rather than retained during contact with Al_2O_3 resulting in greater volumetric loss than track morphology.

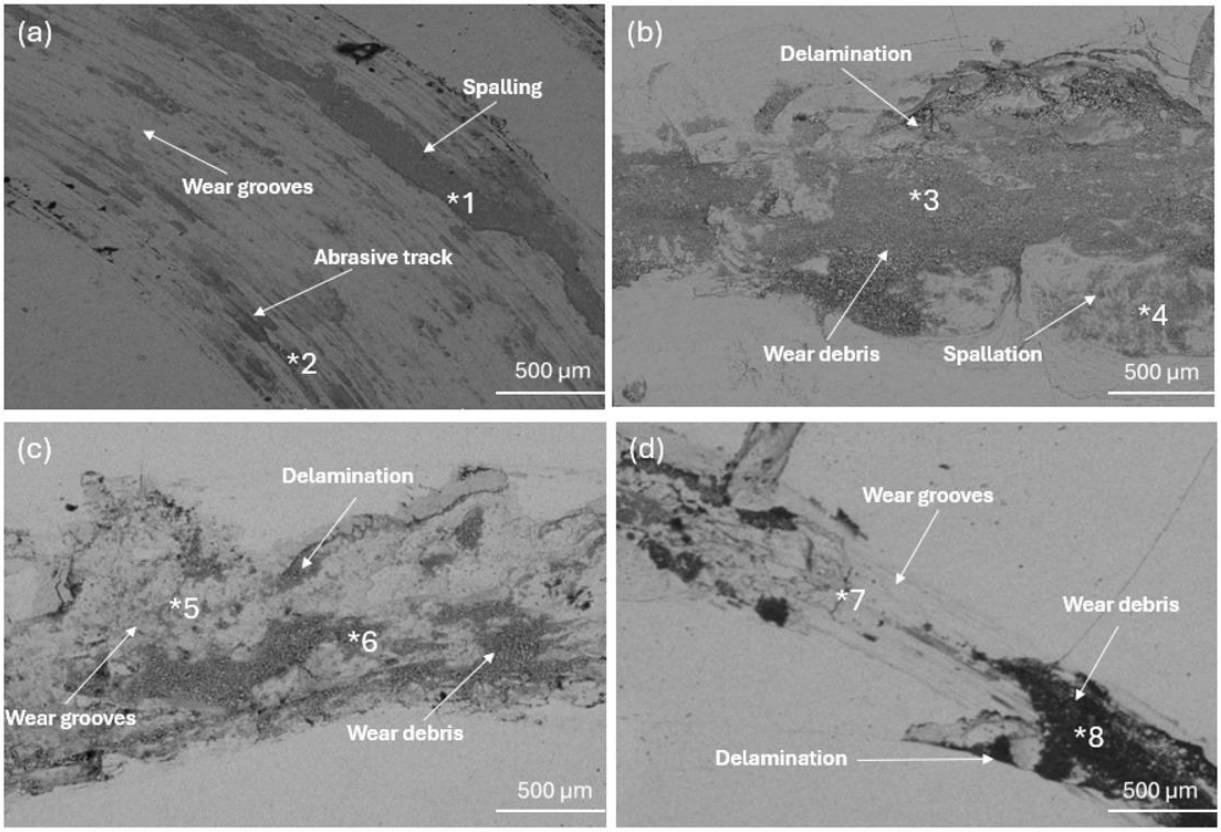

Figure 9. Wear scar of (**a**) Ti6Al4V, (**b**) HEA 1, (**c**) HEA 2, and (**d**) HEA 3at a load of 5 N with EDS spot analysis for Ti6Al4V (*1, *2), HEA 1 (*3, *4), HEA 2 (*5, *6) and HEA 3 (*7, *8).

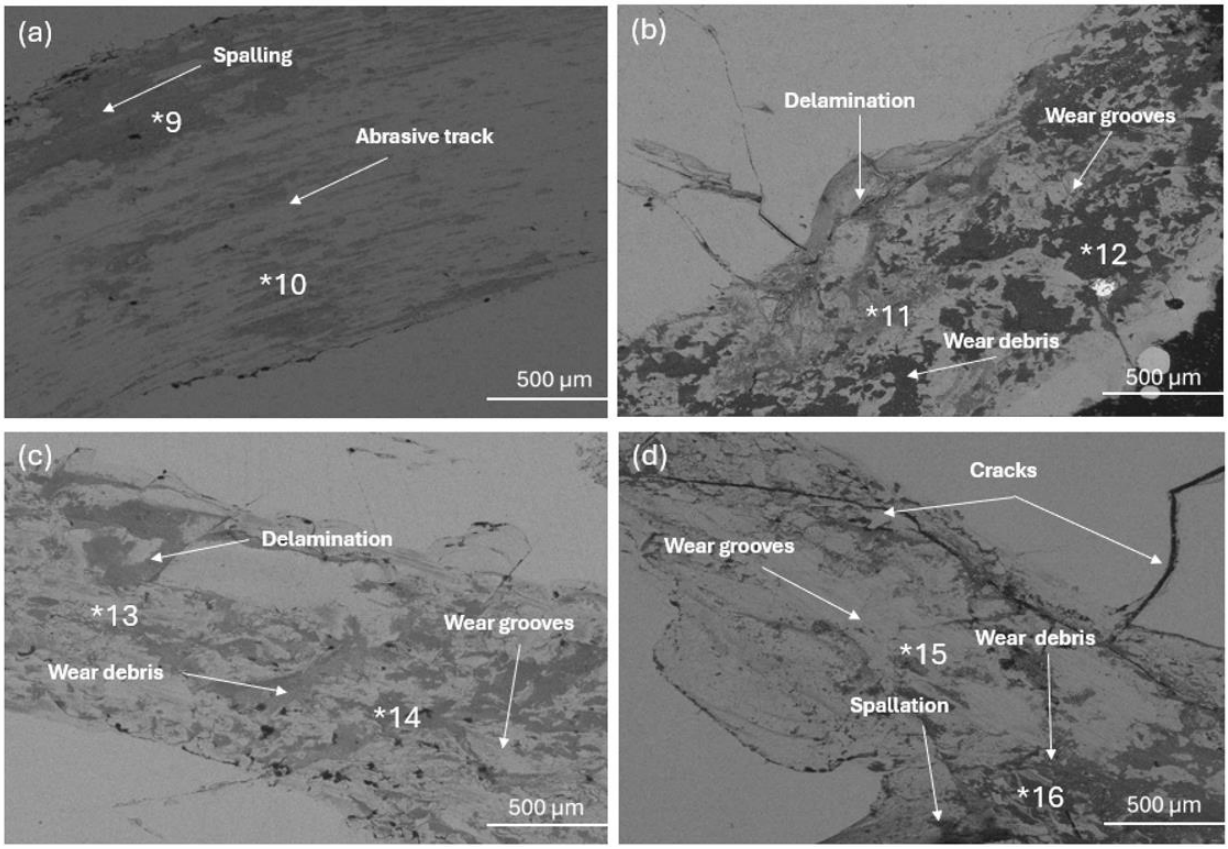

Figure 10. Wear scar of (**a**) Ti6Al4V, (**b**) HEA 1, (**c**) HEA 2, and (**d**) HEA 3 at a load of 15 N with EDS spot analysis for Ti6Al4V (*9, *10), HEA 1 (*11, *12), HEA 2 (*13, *14) and HEA 3 (*15, *16).

Table 5. EDS spot analysis (at%) of the worn surfaces/wear debris at 5 N and 15 N.

Load	Material	Point	O	Ti	Al	Si	Cr	Co	V
5 N	Ti6Al4V	1	44.5	48.3	4.9	-	-	-	2.3
		2	63.3	27.5	6.5	-	-	-	2.7
	HEA 1	3	15.5	19.4	18.5	13.8	16.7	14.5	1.6
		4	19.6	20.7	16.6	15.9	13.7	13.3	0.2
	HEA 2	5	5.3	9.2	8.3	7.8	35.4	33.5	0.5
		6	19.4	8.2	8.2	8.5	28.8	26.5	0.4
	HEA 3	7	3.5	35.3	34.8	7.6	9.5	8.8	0.5
		8	25.3	27.2	22.2	8.3	8.5	7.8	0.7
15 N	Ti6Al4V	9	35.2	55.3	6.2	-	-	-	3.3
		10	33.3	58.2	5.3	-	-	-	3.2
	HEA 1	11	18.5	19.4	17.6	14.6	15.4	14.1	0.4
		12	17.3	20.2	16.3	14.3	15.2	16.3	0.4
	HEA 2	13	9.4	7.8	6.9	8.7	34.2	32.3	0.7
		14	17.6	8.4	8.3	8.6	29.4	24.1	0.4
	HEA 3	15	9.5	33.8	31.6	7.5	8.3	8.8	0.5
		16	29.4	22.6	21.4	8.6	9.2	8.4	0.4

The Ti6Al4V substrate at 15 N displays a broader and more heavily damaged abrasive track relative to 5 N with pronounced spalling extending across a larger fraction of the track area. The abrasive grooves remain the primary damage feature, but their increased density and the extensive spalling indicate that the contact stress at 15 N exceeds the threshold for pure mild abrasive wear and material removal by spallation. This observation is consistent with Archard's law prediction that wear volume is with load and agrees with the substrate's higher wear rate at these conditions. HEA 1 at 15 N shows the most severe coating damage of the HEA compositions at this load. The severe wear is characterized by extensive delamination with large flakes, wear grooves, and a broad debris-covered track. Despite the morphological damage of the worn surface, HEA 1 still maintained a lower wear rate than the uncoated substrate at 15 N, indicating the hardness advantage of the coating continues to limit material loss even when the dominant mechanism shifts from mild delamination to severe damage. Whereas HEA 2 at 15 N exhibits delamination, wear grooves, and a debris accumulation, the damaged region appears less extensive than that observed in HEA 1. The track has partial delamination retained with shallow grooves, and debris layer is visible within the track. This morphology is consistent with the formation of a protective oxide layer Cr_2O_3 which surpasses direct penetration and limits the extent of delamination. The ability of HEA 2 to sustain the Cr_2O_3 oxide layer at 15 N correlates with its lowest CoF among all specimens at this load (0.26) and supports the attribution of frictional reduction to an oxide-based mechanism for this HEA 2 composition. Finally, the HEA 3 at 15 N presents the most complex and severe morphology among the HEA coatings, exhibiting grooves, surface cracks, wear debris, and spallation. The presence of cracks, a feature not observed at 5 N, indicates that the 15 N load exceeds the fracture initiation threshold of the Al/Ti-enriched coating. This is consistent with the relatively low fracture toughness of the Al/Ti intermetallic phases ($AlTi_3$, $Al_{13}Co_4$) identified by XRD, whose brittle character makes crack propagation favourable under cyclic contact loading. The spalling associated with cracks produces large debris particles that act as third-body abrasives, further accelerating surface damage and wear rate. Overall, the worn surface analysis confirms that all HEA coatings shift the dominant wear mechanism away from the abrasive grooving and spalling that characterises Ti6Al4V. At 5 N, the hard HEA coatings resist micro-cutting and localise delamination damage, giving lower wear rates than the substrate. At 15 N, delamination worsens for HEA 1 and HEA 3, though the coatings still outperform the uncoated substrate. HEA 2 stands out by maintaining partial oxide layer formation even at 15 N, which limits delamination and delivers the low wear rate and low CoF at higher loads. These surface observations align with quantitative wear and friction presented in Section 3.4.

Elevated O content at the worn surface points relative to the as-deposited regions (Table 3, 0% O) is consistent with a partially oxidized debris layer. HEA 2 debris points additionally retain a high proportion of Cr alongside O, which suggests a Cr_2O_3 protective layer mechanism proposed in Section 3.4. Whereas HEA 3 shows high O content at 15 N without a Cr signature seen in HEA 2, this is consistent with HEA 3's Al/Ti intermetallic and with the debris expulsion behaviour rather than the formation of a stable, adherent oxide layer.

4. Conclusions

This study investigated the effect of compositional variation within the AlTiSiCrCo HEA family on microstructure, hardness, and dry sliding wear behaviour of laser cladded coatings on Ti6Al4V. The following conclusions are drawn:

- All three coatings were metallurgically bonded to the substrate and consisted of a BCC solid solution matrix reinforced by intermetallic precipitates. XRD analysis confirmed

that HEA 1 formed $AlSi_3Ti_2$, Cr_2Ti, $Al_{13}Co_4$, and a BCC phase; HEA 2 formed a predominant BCC structure with secondary $AlCr_2$ and $AlTi_3$; and HEA 3 produced $Al_{13}Co_4$, $AlCr_2$, $AlTi_3$ with BCC. Phases identified from a single diffraction reflection should be regarded as tentative pending further characterization. Phase constitution was determined by thermodynamic balance between configurational entropy and mixing entropy.

- All HEA coatings exhibited substantially higher hardness than the Ti6Al4V substrate (345 HV). The hardness ranking HEA 2 (755.1 HV) > HEA 3 (754.2 HV) > HEA 1 (705.1 HV) reflects the synergistic contribution of BCC solid solution strengthening and dispersion hardening by hard intermetallic phases.
- All three coatings outperformed Ti6Al4V in dry sliding wear at both 5 N and 15 N. SEM worn surface analysis revealed that the dominant wear for HEA coatings at 5 N was delamination, replacing the abrasive grooves that characterise the Ti6Al4V. At 15 N, delamination intensified for HEA 1 and HEA 3, which escalated to severe damage involving cracking and spallation, while HEA 2 partially sustained a Cr_2O_3 oxide layer. This is directly supported by the elevated Cr and O content retained at the HEA 2 worn surface (Table 5). The oxide layer limits the delamination and delivers the lowest rate at both loads 4.570×10^{-5} $mm^3/N.m$ at 5 N and 2.74×10^{-4} $mm^3/N.m$. Wear at 5 N was governed by mild oxidative mechanism, transitioning to combined abrasive and adhesive wear at 15 N. This transition is corroborated quantitatively by the Archard wear coefficient (Table 4), which remained in the $10^{-4} - 10^{-3}$ range at both loads and was lower for HEA 2.
- The tribological performance ranking HEA 2 > HEA 3 > HEA 1 was maintained across both loads demonstrating that Cr/Co enrichment within the AlTiSiCrCo system is the most effective compositional strategy for enhancing the wear performance of laser cladded coatings on Ti6Al4V for demanding surface engineering applications.

Author Contributions: Conceptualization, K.M.R.; Methodology, K.M.R., N.W.M. and S.S.; Validation, N.W.M.; Formal analysis, N.W.M.; Investigation, K.M.R.; Resources, N.W.M. and S.S.; Writing—original draft preparation, K.M.R.; Writing—review and editing, M.E.M. and N.W.M.; Visualization, K.M.R.; Supervision, M.E.M., N.W.M. and S.S.; Project administration, M.E.M. All authors have read and agreed to the published version of the manuscript.

Funding: This research received no external funding.

Data Availability Statement: Data are contained within this article.

Conflicts of Interest: The authors declare no conflict of interest.

References

1. Zhong, C.; Liu, J.; Zhao, T.; Schopphoven, T.; Fu, J.; Gasser, A.; Schleifenbaum, J.H. Laser metal deposition of Ti6Al4V—A brief review. *Appl. Sci.* **2020**, *10*, 764. [CrossRef]
2. Lin, N.; Li, D.; Zou, J.; Xie, R.; Wang, Z.; Tang, B. Surface texture-based surface treatments on Ti6Al4V titanium alloys for tribological and biological applications: A mini review. *Materials* **2018**, *11*, 487. [CrossRef] [PubMed]
3. Philip, J.T.; Mathew, J.; Kuriachen, B. Tribology of Ti6Al4V: A review. *Friction* **2019**, *7*, 497–536. [CrossRef]
4. Kumar, V.; Kumar, R.; Das, A.K. Comprehensive study of process parameters and their effect on tribological properties of laser cladded Ti6Al4V alloy: A review. *Mater. Today Proc.* **2024**, *98*, 91–96. [CrossRef]
5. Liu, Y.; Ding, Y.; Yang, L.; Sun, R.; Zhang, T.; Yang, X. Research and progress of laser cladding on engineering alloys: A review. *J. Manuf. Process.* **2021**, *66*, 341–363. [CrossRef]
6. Okoli, U.O.; Otunniyi, I.O.; Adebiyi, I.D. Dry sliding wear behaviour of binary powder laser cladded Ti-6Al-4V using SiC and Al. *Mater. Today Proc.* **2021**, *38*, 988–993. [CrossRef]
7. Adesina, O.S.; Popoola, A.P.; Farotade, G.A.; Obadele, B.A.; Sanyaolu, O.O.; Jeje, S.O.; Rominiyi, A.L. Effect of SiC addition on laser-based CoNi binary alloy coatings on Ti-6Al-4V alloy. *Emergent Mater.* **2024**, *7*, 2117–2128. [CrossRef]

8. Wang, K.; Zhang, Z.; Xiang, D.; Ju, J. Research and Progress of Laser Cladding: Process, Materials and Applications. *Coatings* **2022**, *12*, 1382. [CrossRef]
9. Siddiqui, A.A.; Dubey, A.K. Recent trends in laser cladding and surface alloying. *Opt. Laser Technol.* **2021**, *134*, 106619. [CrossRef]
10. Prakash, O.; Chandrakar, R.; Martin, L.; Verma, J.; Kumar, A.; Jaiswal, A. Laser Cladding Technology for High Entropy Alloys: Effect and Applications. *Mater. Res. Express* **2024**, *11*, 096510. [CrossRef]
11. Wen, H.M.; Pang, M.; Hu, Y.J. Study on fabrication of multi-phase reinforcement coatings on Ti6Al4V by laser cladding for enhanced tribological performance. *Mater. Today Commun.* **2024**, *41*, 110566. [CrossRef]
12. Adesina, O.S.; Popoola, A.P.I.; Pityana, S.L.; Oloruntoba, D.T. Microstructural and tribological behavior of in situ synthesized Ti/Co coatings on Ti-6Al-4V alloy using laser surface cladding technique. *Int. J. Adv. Manuf. Technol.* **2018**, *95*, 1265–1280. [CrossRef]
13. Zhang, B.; Hua, X.; Yang, F. Study on Wear and Corrosion Resistance of Co-Cr-Ti Composite Coatings on Ti6Al4V by Laser Cladding. *JOM* **2025**, *77*, 4862–4876. [CrossRef]
14. Poulia, A.; Karantzalis, A.E. Latest Advancements and Mechanistic Insights into High-Entropy Alloys: Design, Properties and Applications. *Materials* **2025**, *18*, 5616. [CrossRef] [PubMed]
15. Cantor, B.; Chang, I.T.H.; Knight, P.; Vincent, A.J.B. Microstructural development in equiatomic multicomponent alloys. *Mater. Sci. Eng. A* **2004**, *375–377*, 213–218. [CrossRef]
16. Yeh, J.W. Physical Metallurgy of High-Entropy Alloys. *JOM* **2015**, *67*, 2254–2261. [CrossRef]
17. Ye, Y.; Wang, Q.; Lu, J.; Liu, C.; Yang, Y. High-entropy alloy: Challenges and prospects. *Mater. Today* **2016**, *19*, 349–362. [CrossRef]
18. Xie, H.; Tong, Y.; Bai, Y.; Li, X.; Han, Y.; Hua, K.; Wang, H. Wear-Resistance of High-Entropy Alloy Coatings and High-Entropy Alloy-Based Composite Coatings Prepared by the Laser Cladding Technology: A Review. *Adv. Eng. Mater.* **2023**, *25*, 2300426. [CrossRef]
19. Arif, Z.U.; Khalid, M.Y.; Rehman, E.U.; Ullah, S.; Atif, M.; Tariq, A. A review on laser cladding of high-entropy alloys, their recent trends and potential applications. *J. Manuf. Process.* **2021**, *68*, 225–273. [CrossRef]
20. Xiong, W.; Cheng, L.; Zhan, S.; Guo, A.X.Y.; Liaw, P.K.; Cao, S.C. Recent Advances on Lightweight High-Entropy Alloys: Process, Design, and Applications. *High Entropy Alloy. Mater.* **2023**, *1*, 175–194. [CrossRef]
21. Meng, Y.; Yang, Z.; Shi, Y.; Liu, X.; Wang, L.; Zhang, Q.; Yao, J. Microstructural evolution and enhanced properties of multi-layer TiZrNbCrCo high entropy alloy coatings laser-clad onto Ti–6Al–4V alloy. *Intermetallics* **2024**, *173*, 108407. [CrossRef]
22. Prabu, G.; Duraiselvam, M.; Jeyaprakash, N.; Yang, C.H. Microstructural Evolution and Wear Behavior of AlCoCrCuFeNi High Entropy Alloy on Ti–6Al–4V Through Laser Surface Alloying. *Met. Mater. Int.* **2021**, *27*, 2328–2340. [CrossRef]
23. Ren, Z.Y.; Hu, Y.L.; Tong, Y.; Cai, Z.H.; Liu, J.; Wang, H.D.; Liao, J.Z.; Xu, S.; Li, L.K. Wear-resistant NbMoTaWTi high entropy alloy coating prepared by laser cladding on TC4 titanium alloy. *Tribol. Int.* **2023**, *182*, 108366. [CrossRef]
24. Raselabe, K.M.; Makhatha, E.M.; Makoana, W.; Skhosane, S. Response surface methodology-based optimization of laser cladding parameters for hardness of AlTiSiCrCo coated Ti6Al4V. *Eng. Res. Express* **2025**, *7*, 045506. [CrossRef]
25. Huang, C.; Zhang, Y.; Vilar, R.; Shen, J. Dry sliding wear behavior of laser clad TiVCrAlSi high entropy alloy coatings on Ti–6Al–4V substrate. *Mater. Des.* **2012**, *41*, 338–343. [CrossRef]
26. Li, R.; Yu, W.; Zhang, Y.; Li, C.; Qu, Y.; Nie, S.; Tian, C.; Tan, B.; Yu, B. Effect of Phase Proportion on Wear Behavior of Al–Cr–Fe–Ni Dual-Phase High Entropy Alloys. *Met. Microstruct. Anal.* **2021**, *10*, 106–115. [CrossRef]
27. Cheng, C.Y.; Yang, Y.C.; Zhong, Y.Z.; Chen, Y.Y.; Hsu, T.; Yeh, J.W. Physical metallurgy of concentrated solid solutions from low-entropy to high-entropy alloys. *Curr. Opin. Solid State Mater. Sci.* **2017**, *21*, 299–311. [CrossRef]
28. Senkov, O.N.; Miracle, D.B. A new thermodynamic parameter to predict formation of solid solution or intermetallic phases in high entropy alloys. *J. Alloys Compd.* **2016**, *658*, 603–607. [CrossRef]
29. Raselabe, K.M.; Makhatha, M.E.; Mokoana, W.; Skhosane, S. Tribological performance of laser-clad AlTiSiCrCo high-entropy alloy coating on Ti6Al4V substrate. *Eng. Res. Express* **2026**, *8*, 065404. [CrossRef]
30. Lu, K.; Zhu, J.; Guo, D.; Yang, M.; Sun, H.; Wang, Z.; Hui, X.; Wu, Y. Microstructures, Corrosion Resistance and Wear Resistance of High-Entropy Alloys Coatings with Various Compositions Prepared by Laser Cladding: A Review. *Coatings* **2022**, *12*, 1023. [CrossRef]
31. Chen, B.; Li, S.; Ding, J.; Ding, X.; Sun, J.; Ma, E. Correlating dislocation mobility with local lattice distortion in refractory multi-principal element alloys. *Scr. Mater.* **2023**, *222*, 115048. [CrossRef]
32. Juan, Y.; Li, J.; Jiang, Y.; Jia, W.; Lu, Z. Wear-resistant single-phase high-entropy alloy coatings prepared on Ti6Al4V with laser cladding. *Wear* **2019**, *53*, 751–758. [CrossRef]
33. Liang, H.; Hou, J.; Liu, J.; Xu, H.; Li, Y.; Jiang, L.; Cao, Z. The Microstructures and Wear Resistance of $CoCrFeNi_2Mo_x$ High-Entropy Alloy Coatings. *Coatings* **2024**, *14*, 760. [CrossRef]

34. Zhang, H.-T.; Wang, C.-L.; Miao, J.-W.; Shi, S.-Y.; Li, T.-J.; Yan, H.-W.; Zhang, Y.-A.; Lu, Y.-P. Effect of microstructure evolution on wear resistance of equal molar CoCrFeNi high-entropy alloy. *Rare Met.* **2023**, *42*, 3797–3805. [CrossRef]
35. Lu, Y.; Peng, Y.; Chang, X.; Xiu, W.; Shi, Z. Insights on microstructure and tribological properties of FeCoCrNiMo HEA reinforced CuSn coatings by laser cladding for monorail brakes. *Wear* **2025**, *580–581*, 206244. [CrossRef]